Optics Letters

Tunable Janus absorptive frequency-selective reflector with octave frequency absorption

Zhao Tang,† Si-Ying Li,† Jie Xu, and Hai-Feng Zhang*

College of Electronic and Optical Engineering & College of Flexible Electronics (Future Technology), Nanjing University of Posts and Telecommunications, Nanjing 210023, China
† *These authors contributed equally to this Letter.*
**hanlor@163.com*

Received 20 July 2023; revised 26 July 2023; accepted 26 July 2023; posted 27 July 2023; published 14 August 2023

A tunable Janus absorptive frequency-selective reflector (AFSR) utilizing a graphene-based hyperbolic that showcases exceptional doubling octave frequency absorption (DOFA) or tripling octave frequency absorption (TOFA) is proposed. The multi-objective gray wolf optimization algorithm is employed to drive the transfer matrix method, optimizing parameters such as the dielectric permittivity, thickness, and the Fermi level (E_f) to achieve harmonic absorption. By manipulating the E_f of graphene, the dimensions of the absorption band and reflection window can be finely adjusted. Additionally, a frequency-selective reflector is introduced, enabling a seamless transition between selective absorption and transmission by adjusting the E_f. This AFSR represents a groundbreaking approach to achieving DOFA or TOFA while simultaneously offering valuable insights into the design of intelligent AFSRs.

https://doi.org/10.1364/OL.501274

The absorptive frequency-selective reflector (AFSR), a device that exhibits both frequency selectivity and absorptive properties, was first proposed by Omar *et al.* in 2017 [1]. The AFSR reflects electromagnetic waves (EWs) within a specific frequency band while absorbing EWs on both sides of the reflection band, thus offering significant advantages in applications such as reducing radar cross sections and enhancing signal quality and reliability in communication systems. Since its initial introduction, the design of the AFSR has undergone continuous improvements [2]. In 2020, Zhang *et al.* [3] proposed a dual-polarized AFSR with wide reflection and absorption bands. Guo *et al.* [4] devised an AFSR with an ultrawide reflection band ranging from 8.94 to 15.1 GHz, which meets the demand for a wider operating bandwidth in radar and communication systems. In 2023, Fan *et al.* [5] proposed a dual-polarization AFSR with an adjustable reflective band; this tunability could contribute to the design of intelligent antenna reflector systems. The AFSRs mentioned above were all demonstrated experimentally by those researchers.

The term "Janus" is used to refer to a structure that possesses distinct properties in two directions. In this Letter, the Janus characteristic is the contrasting absorption behaviors of forward-propagating electromagnetic waves (FPEWs) and backward-propagating electromagnetic waves (BPEWs) upon entering the device. To vividly express the Janus feature, the concept of isolation is introduced. The isolation, denoted as S, is given by $S = |A - oppA|$, where A and $oppA$ are the absorption of FPEWs and BPEWs, respectively. $S > 0.8$ is the threshold for the Janus property [6]. Doubling octave frequency absorption (DOFA) or tripling octave frequency absorption (TOFA) refers to the phenomenon where a structure displays high absorption both in a specific frequency region and in its corresponding doubling or tripling octave frequency interval while manifesting significant reflection in the intermediate range between the two absorption bands. This distinction has extensive applications in military signal encryption, the absorption of the second harmonic [7], intelligent stealth coatings, and other fields. Some studies on the design of two-octave coatings have been reported. In 2011, the optimal dual-component antireflection coatings for an ultra-broadband (UWB) spectral range was investigated [8]. In 2014, the feasibility of precision dispersive mirror systems spanning two octaves was demonstrated [9]. Dispersive mirrors that operate in a broadband infrared spectral range and can provide group delay dispersions of -100 fs^2 and -200 fs^2 in this range were reported in 2019 [10].

The one-dimensional (1D) photonic bandgap structure (PBS) is famous for generating a photonic bandgap (PBG) [11]. In this Letter, a 1D PBS is utilized as the physical model of the AFSR and the PBG serves as the reflection window for the AFSR. On either side of the PBG, a graphene-based hyperbolic metamaterial (GHM) embedded in PBS efficiently absorbs the incident EWs [12]. Notably, the absorption intervals adjacent to the PBG exhibit intriguing relationships with a doubling or tripling factor. Given the critical influence of the parameter selection for the PBS on device functionality, the multi-objective gray wolf optimizer (MOGWO) is employed to drive the transfer matrix method (TMM) which optimizes the dielectric constants, thicknesses, and the Fermi level (E_f) of the media in the PBS. MOGWO is a multi-objective optimization algorithm proposed by Mirjalili *et al.* in 2016 [13] which has shown extraordinary search and convergence ability in the optimization of many complex engineering problems. Significantly, the primary emphasis of this Letter is not on the investigation of algorithms. In this Letter, a Janus AFSR with DOFA or TOFA is achieved. The variable K represents the ratio between the lower cutoff frequency of the second absorption interval (fl_2) and the lower

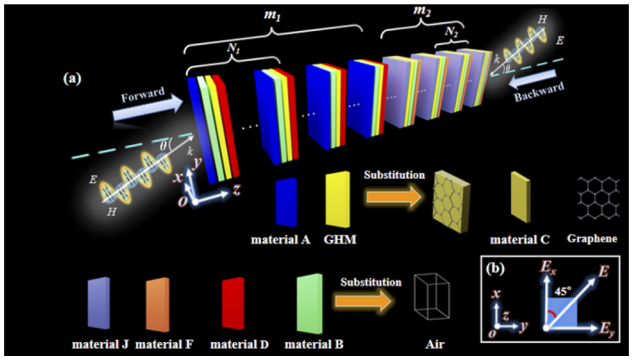

Fig. 1. (a) Schematic view of the composite PBS consisting of periodic sequences $((\text{A-B-GHM-D})^{N1})^{m1}$-$((\text{J-GHM-B-F})^{N2})^{m2}$. (b) Front view of the incident mode of the EWs through the PBS.

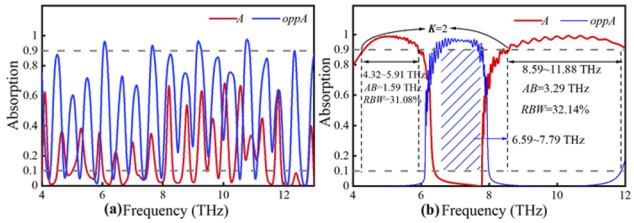

Fig. 2. Absorption spectra of EWs through the LSP with MOGWO iterated (a) one time and (b) 1000 times.

cutoff frequency of the first absorption interval (fl_1) . In the case of DOFA, K is approximately 2, with $2fl_1$ exceeding fl_2. Similarly, for TOFA, K is roughly 3, with $3fl_1$ greater than fl_2. Moreover, applying various bias voltages [14] enables the absorption and reflection bands to be tuned by modulating E_f. Additionally, a reflector capable of switching between selective absorption and transmission is developed by varying the E_f.

The proposed PBS is illustrated in Fig. 1(a). Figure 1(b) displays a frontal view of the incident mode of EWs through the PBS. The electric field direction of the incident EWs is parallel to the x-y plane and is at 45° with respect to the x axis. Therefore, it can be decomposed into E_x and E_y components pointing along the x axis and y axis, respectively. These two mutually perpendicular electric fields denote transverse electric (TE) and transverse magnetic (TM) waves [15], indicating that the incident wave is linearly polarized. Due to the favorable propensity for PBG generation within periodic sequences, two distinct periodic sequences are meticulously formulated and deployed within the anterior and posterior segments of the PBS, respectively. The GHM is composed of dielectric C and graphene, and the thickness of graphene is 0.345 nm. The materials A and D, the air layer (B), and the GHM are arranged in a specific order: A-B-GHM-D, forming a unit sequence denoted as P_1. Then the unit sequence P_1 is repeated N_1 times to form $P_1P_1\ldots P_1 = (P_1)^{N1}$, with all GHM layers having the same E_f. Furthermore, $(P_1)^{N1}$ is repeated m_1 times to construct the front half of the AFSR, which is denoted as $((\text{A-B-GHM-D})^{N1})^{m1}$. Notably, there are m_1 sections of $(P_1)^{N1}$, where the GHM layers within each $(P_1)^{N1}$ have the same E_f but the E_f values of GHM layers differ among different $(P_1)^{N1}$ sections. Upon varying the E_f under different $(P_1)^{N1}$ values, the absorption capability of the graphene varies, significantly expanding the search space of MOGWO and providing a basis for selective absorption. Similarly, the rear segment of the PBS incorporates a periodic structure comprising materials J and F, and B and the GHM arranged in the sequence $((\text{J-GHM-B-F})^{N2})^{m2}$, which is connected to the preceding structure. As a result, the overall sequence of the PBS is $((\text{A-B-GHM-D})^{N1})^{m1}$–$((\text{J-GHM-B-F})^{N2})^{m2}$. The layer count for A and D corresponds to $N_1 \cdot m_1$, while that for J and F is equal to $N_2 \cdot m_2$. Additionally, the number of layers for B and GHM is $N_1 \cdot m_1 + N_2 \cdot m_2$. The EWs and coordinate axes are depicted in Fig. 1(a), where the positive direction of the z axis represents the forward propagation of EWs, and the $-z$-axis direction denotes the backward propagation. θ is the angle of incidence. Without a loss of generality, the structure is placed in the air at a working temperature of 300 K and with a phenomenological scattering rate of 10^{-13} s [6]. The relative dielectric constants of materials A, C, D, J, and F are denoted by ε_a, ε_c, ε_d, ε_j, and ε_f, respectively, and their thicknesses are represented by d_A, d_C, d_D,d_J, and d_F, respectively. The thickness of B is indicated as d_B. The parameters mentioned above (including the E_f of the GHM), treated as the independent variables in the objective function, are optimized by MOGWO. Since N_1, m_1, N_2, and m_2 are discrete positive integers, an enumeration method is utilized to determine their values. These values are manually adjusted according to the corresponding optimized outcomes, leading to a significant reduction in computational complexity (see Part 6 of the Supplement 1). How to fabricate such a PBS and the way to modulate the E_f are described in Parts 4 and 5 of the Supplement 1, respectively.

To get the desired Janus AFSR with DOFA, the parameters of the sequence $((\text{A-B-GHM-D})^{N1})^{m1}$–$((\text{J-GHM-B-F})^{N2})^{m2}$ are optimized (see Part 3 of the Supplement 1). Initially, two absorption intervals with a multiple relationship are selected, and the intermediate region between them is designated as the reflection band. Subsequently, the absorption and reflectivity of EWs are calculated by the TMM at vertical incidence ($\theta = 0°$) (see Part 1 of the Supplement 1). To expand the absorption and reflection bandwidths, MOGWO is used to optimize the parameters (see Part 2 of the Supplement 1).

Figure 2(a) presents an absorption plot for the PBS after a single iteration of MOGWO, which is used as a control group. Under the periodic sequence, the absorption curves of both FPEWs and BPEWs exhibit numerous absorption peaks, resulting in a poor absorption bandwidth and a lack of DOFA due to energy localization induced by the inclusion of defective layers (B), leading to the emergence of multiple PBGs. After 1000 iterations of MOGWO, the Janus AFSR with DOFA ($K = 2$) is achieved, as shown in Fig. 2(b). In Fig. 2(b), for the FPEWs, the AFSR achieves Janus UWB absorption in the intervals 4.32–5.91 THz and 8.59–11.88 THz, with a relative bandwidth (*RBW*) of 31.08% and 32.14%, respectively. Between the absorption intervals, the presence of the PBG enables perfect selectivity of the AFSR. $K = 2$ signifies the implementation of DOFA, which is credited to the favorable impedance matching within the absorption intervals and the strategic positioning of the PBG between the absorption bands. The absorption curve for the BPEWs is depicted by the blue line in Fig. 2(b), with the absorption interval positioned opposite to that of absorption for FPEWs and distributed from 6.59 to 7.78 THz. Two UWB reflection windows are observed on both sides; these result from the significant refractive index difference between media J and F. Ultimately, the positions of the absorption intervals and reflection regions in the two curves are inverted, signifying the desired Janus feature. In Fig. 2(b), the absorption and

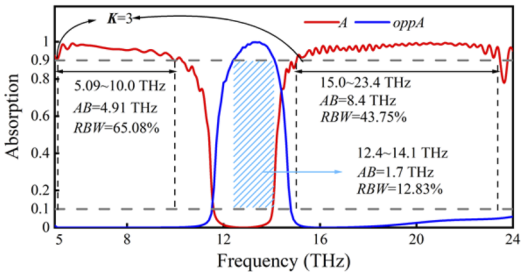

Fig. 3. Absorption plot of the Janus AFSR with TOFA.

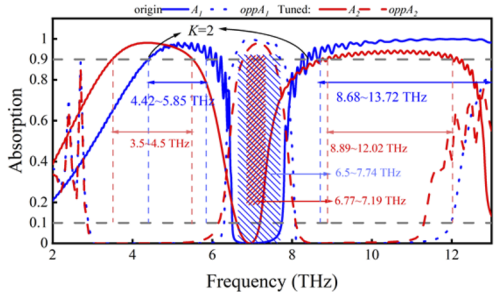

Fig. 4. Absorption of the tunable Janus AFSR.

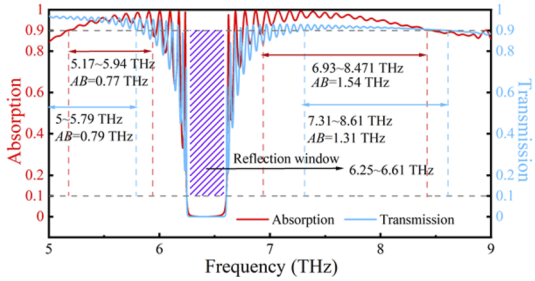

Fig. 5. Absorption of the AFSR and the transmission of the TFSR.

reflection intervals for FPEWs and BPEWs are inverted, resulting in significantly reduced transmittance. This indicates that the EWs encounter substantial obstacles when traversing the Janus AFSR. The anterior segment $((\text{A-B-GHM-D})^{N1})^{m1}$ and the posterior part $((\text{J-GHM-B-F})^{N2})^{m2}$ govern, respectively, the absorption and reflection of FPEWs and BPEWs while exhibiting minimal coupling effects between the two structures. This pattern of *A* and *oppA* remains consistent in subsequent results for the Janus AFSR.

Moreover, taking into account the unique application potential of selective absorption at various octaves, the aim is further refined to encompass the attainment of TOFA ($K = 3$). With the objective function adjusted, the dielectric constants and thicknesses of the materials in $((\text{A-B-GHM-D})^{N1})^{m1}$–$((\text{J-GHM-B-F})^{N2})^{m2}$ are optimized (the relevant parameters can be found in Part 3 of the Supplement 1). The absorption plot for EWs at the Janus AFSR with TOFA is displayed in Fig. 3. For the FPEWs, the absorption area is enormously expanded owing to impedance matching between the PBS and free space within 5.09–10 THz and 15–23.4 THz, and the *RBW* values are 65.08% and 43.75%, respectively. With $fl_1 = 5.09$ THz and $fl_2 = 15$ THz, *K* approaches 3, representing exceptional TOFA. The Janus window within 12.4–14.1 THz with $A < 0.1$ and $oppA > 0.9$ is responsible for the selective functionality of AFSR.

To enhance the flexibility of the AFSR and adapt it to complex usage scenarios, a tunable Janus AFSR with DOFA is achieved by changing the E_f. The absorption before the regulation is denoted as A_1 for the FPEWs and $oppA_1$ for the BPEWs, while A_2 and $oppA_2$ represent the absorption after modification. The absorption of the AFSR is presented in Fig. 4. (The optimized parameters can be found in Part 3 of the Supplement 1.) Before the adaptation, the two absorption intervals for FPEWs span from 4.42 to 5.85 THz and from 8.68 to 13.72 THz with the realization of DOFA. After the adjustment, the first absorption interval undergoes an overall redshift, and the absolute bandwidth (*AB*) increases from 1.43 THz to 2 THz. The second absorption interval shows a reduction in *AB*, which decreases from 5.04 THz to 3.13 THz. The *AB* of the Janus window, which satisfies $oppA > 0.9$ and $A < 0.1$, shrinks from 1.24 THz to 0.42 THz. In summary, flexible regulation of the E_f enables the functionality of the system to be manipulated.

Furthermore, the versatile electrostatic modulation capability of the GHM enables the creation of a versatile reflector capable of seamlessly transitioning between an AFSR and a transmissive frequency selective reflector (TFSR). Disregarding the DOFA and Janus property, the optimization is focused solely on the relevant parameters of the PBS comprising $((\text{A-B-GHM-D})^{N1})^{m1}$. In Fig. 5, the absorption of the AFSR and transmission of the TFASR are illustrated. (Information on the A, B, GHM, and D layers are available in Part 3 of the Supplement 1.) In Fig. 5, while maintaining a consistent reflection window within 6.25–6.61 THz, broad conversion ranges that are capable of switching between absorption and transmission are achieved on both sides. Specifically, before changing the E_f of the GHM, the left side of the reflection window exhibits an absorption bandwidth of 0.77 THz, while the *AB* of the absorption region on the right side is 1.54 THz. Upon adjusting the E_f, high-transmission regions are observed within 5–5.79 THz and 7.31–8.61 THz. There are two overlaps between the absorption bands and the transmission intervals, enhancing the application value of this PBS. This phenomenon can be attributed to the augmented E_f, which leads to hindered electron transitions within graphene, consequently restricting the absorption capacity and promoting abundant EW transmission [16].

Considering the differential impacts of changes in d_A and d_D on *A*, as well as the effects of varying d_J and d_F on *oppA*, it is important to further explore these aspects. The outcomes of the Janus AFSR with different values of d_A, d_D, d_J, and d_F and the other conditions kept constant are illustrated in Fig. 6. The results indicate that the thicknesses of these four media significantly affect the selective absorption of DOFA, leading to variations in the position and quantity of the PBG. In Figs. 6(a) and 6(b), a noticeable trend emerges as the thickness of the media increases, with *A* demonstrating a significant deviation from the original DOFA trait. This can be attributed to the impact of thickness variations on the periodicity of PBS, which cause changes in the interference effect of EWs incident at different frequencies, thereby altering the absorption *A* and the position of the PBG. Similarly, in Figs. 6(c) and 6(d), changes in d_J and d_F have a more pronounced impact on the DOFA. The desired DOFA impact exists only under specific conditions, highlighting the powerful search and optimization capability of MOGWO.

The periodic trait of the PBS plays a significant role in facilitating Bragg scattering, thereby exerting a considerable

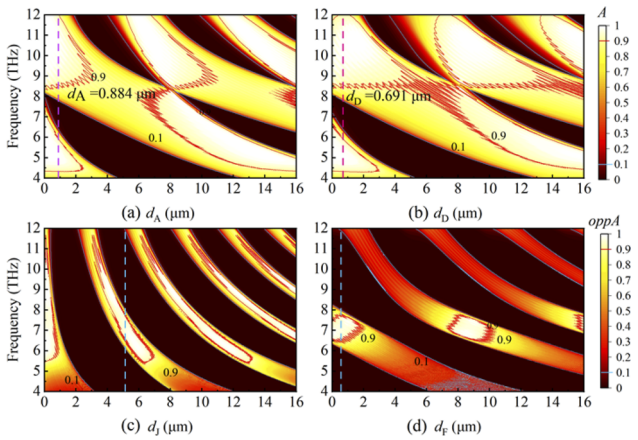

Fig. 6. Variation in the spectrum of the A of FPEWs with (a) d_A and (b) d_D and the variation in the spectrum of the $oppA$ of BPEWs with (c) d_J and (d) d_F.

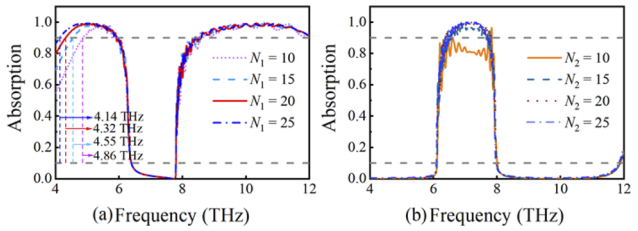

Fig. 7. Absorption profiles of (a) FPEWs with different N_1 and (b) BPEWs with various N_2.

influence on the functionality of the Janus AFSR. Consequently, an investigation is conducted to explore the impact of the period numbers, N_1 and N_2, on the absorption results. Notably, the front and rear segments of the PBS are individually responsible for modulating FPEWs and BPEWs, leading to distinct variations in A and $oppA$ in response to changes in N_1 and N_2 respectively. The corresponding alterations in A and $oppA$ as N_1 and N_2 undergo gradual adjustments are illustrated in Fig. 7, with the gray horizontal lines representing absorptions of 0.9 and 0.1. For the FPEWs, as N_1 increases from 10 to 25, the high-reflection window in the middle remains unchanged between 6.39 and 7.80 THz, while the curve in the latter half remains relatively consistent, with the absorption range remaining around 8.56–11.88 THz. However, in the first absorption interval, as N_1 increases, fl_1 gradually redshifts and the absorption range increases from 4.88 THz to 4.14 THz, because the increase in the number of the resonant structures improves impedance matching. For the BPEWs, Fig. 7(b) illustrates the absorption performance as N_2 varies from 10 to 25. The results indicate that increasing N_2 only affects the absorption within 6–8 THz, while forceful reflection is maintained within 4–6 THz and 8–12 THz, which demonstrates the excellent frequency selectivity of the structure. Specifically, when N_2 is 10, the absorption oscillates between 0.7 and 0.9 within 4–6 THz, falling short of achieving the desired high absorption ($oppA > 0.9$). Upon increasing N_2 from 10 to 25, the absorption region with $oppA > 0.9$ stabilizes at around 6.5–7.8 THz, with only a slight increase in absorption bandwidth. In Table 1, a comparison is made between previously

Table 1. Comparison Between the Proposed AFSR and Others

Refs.	Bandwidth			Properties				
	Absorption (*RBW*)		Reflection (*AB*)	Janus	DOFA	Tunable	Layer Count	Materials
	Left	Right						
[4]	54.1%	24.8%	2.21 THz (3 dB)	No	No	No	2	Metallic Strips
[5]	9%	None	6.16 THz	No	No	No	2	Bent Strip Resonator
[6]	11.3%	54.8%	2.32 THz	No	No	Yes	2	Lossy Layer and Varactor
This Work	31.08%	32.14%	1.26 THz	Yes	Yes	Yes	400	GHM

existing AFSRs and the proposed design. In complex electromagnetic environments, the proposed tunable Janus AFSR with DOFA or TOFA exhibits stronger adaptability and flexibility.

In summary, a tunable Janus AFSR is proposed that exhibits DOFA or TOFA. The tunability of the absorption bandwidth and reflection window is achieved by adjusting the E_f. Furthermore, a frequency-selective reflector was introduced that can be switched between absorption and transmission through the fast electrostatic modulation of graphene. We believe that the present research offers novel insights into the realization of DOFA or TOFA and the design of intelligent AFSRs, and is thus of significant value for future advancements in this field.

Disclosures. The authors declare no conflicts of interest.

Data availability. Data underlying the results presented in this paper are not publicly available at this time but may be obtained from the authors upon reasonable request.

Supplemental document. See Supplement 1 for supporting content.

REFERENCES

1. A. A. Omar, Z. Shen, and H. Huang, IEEE Trans. Antennas Propag. **65**, 6173 (2017).
2. A. A. Omar, H. Huang, and Z. Shen, IEEE Antennas Propag. Mag. **62**, 62 (2020).
3. B. Zhang, C. Jin, and Z. Shen, IEEE Trans. Antennas Propag. **68**, 5736 (2020).
4. T. Guo, M. Guo, X. Jia, Q. Chen, and Y. Fu, IEEE Access **8**, 124217 (2020).
5. Y. Fan, D. Li, H. Ma, J. Xing, Y. Gu, L. K. Ang, and E.-P. Li, IEEE Trans. Antennas Propag. **71**, 2855 (2023).
6. S. Guo, C. Hu, and H. Zhang, J. Opt. Soc. Am. B **37**, 2678 (2020).
7. J. Chen, C.-L. Hu, F. Kong, and J.-G. Mao, Acc. Chem. Res. **54**, 2775 (2021).
8. T. V. Amotchkina, M. K. Trubetskov, V. Pervak, and A. V. Tikhonravov, Appl. Opt. **50**, 6468 (2011).
9. S.-H. Chia, G. Cirmi, S. Fang, G. M. Rossi, O. D. Mücke, and F. X. Kärtner, Optica **1**, 315 (2014).
10. V. Pervak, T. Amotchkina, Q. Wang, O. Pronin, K. F. Mak, and M. Trubetskov, Opt. Express **27**, 55 (2019).
11. M. Butt, S. N. Khonina, and N. Kazanskiy, Opt. Laser Technol. **142**, 107265 (2021).
12. A. Poddubny, I. Iorsh, P. Belov, and Y. Kivshar, Nat. Photonics **7**, 948 (2013).
13. S. Mirjalili, S. Saremi, S. M. Mirjalili, L. d, and S. Coelho, Expert Systems with Applications **47**, 106 (2016).
14. A. N. Grigorenko, M. Polini, and K. Novoselov, Nat. Photonics **6**, 749 (2012).
15. F. Wu, D. Liu, H. Li, and M. Feng, Phys. Chem. Chem. Phys. **25**, 10785 (2023).
16. J. Chen, S. Chen, P. Gu, Z. Yan, C. Tang, Z. Xu, B. Liu, and Z. Liu, Carbon **162**, 187 (2020).